Research in Astronomy and Astrophysics, 22:055012 (12pp), 2022 May https://doi.org/10.1088/1674-4527/ac5bc7
© 2022. National Astronomical Observatories, CAS and IOP Publishing Ltd. Printed in China and the U.K.

Herschel Investigation of Cores and Filamentary Structures in the Perseus Molecular Cloud

Chang Zhang[1,2], Guo-Yin Zhang[1], Jin-Zeng Li[1], and Xue-Mei Li[3]
[1] National Astronomical Observatories, Chinese Academy of Sciences, Beijing 100101, China; zhangc@nao.cas.cn, zgyin@nao.cas.cn, ljz@nao.cas.cn
[2] University of Chinese Academy of Sciences, Beijing 100049, China
[3] College of Physics, Guizhou University, Guiyang 550025, China
Received 2022 January 29; revised 2022 March 1; accepted 2022 March 4; published 2022 April 19

Abstract

Cores and filamentary structures are the prime birthplaces of stars, and play key roles in the process of star formation. Latest advances in the methods of multi-scale source and filament extraction, and in making high-resolution column density map from Herschel multi-wavelength observations enable us to detect the filamentary network structures in highly complex molecular cloud environments. The statistics for physical parameters shows that core mass strongly correlates with core dust temperature, and M/L strongly correlates with M/T, which is in line with the prediction of the blackbody radiation, and can be used to trace evolutionary sequence from unbound starless cores to robust prestellar cores. Crest column densities of the filamentary structures are clearly related with mass per unit length ($M_{\rm line}$), but are uncorrelated by three orders ranging from $\sim 10^{20}$ to $\sim 10^{22}\,{\rm cm}^{-2}$ with widths. Full width at half maximum has a median value of 0.15 pc, which is consistent with the 0.1 pc typical inner width of the filamentary structures reported by previous research. We find 70% of robust prestellar cores (135/199) embedded in supercritical filaments with $M_{\rm line} > 16\,M_\odot\,{\rm pc}^{-1}$, which implies that the gravitationally bound cores come from fragmentation of supercritical filaments. On the basis of observational evidence that the probability distribution function with power-law distribution in the Perseus south is flatter than in the north, the number of young stellar objects in the south is significantly less than that in the north, and dust temperature is different. We infer that the south region is more gravitationally bound than the north region.

Key words: star forming regions – molecular clouds – interstellar filaments

1. Introduction

Molecular clouds (MCs) are dense regions of the cold interstellar medium (ISM), mainly composed of gas and dust, which are the cradles of stars (e.g., Bergin & Tafalla 2007; André et al. 2014; Zhang et al. 2018). Molecular clouds are hierarchical in structure (Men'shchikov et al. 2010; Pokhrel et al. 2018; Men'shchikov 2021b). The substructure of MCs is a complex pattern consisting of filaments, cores, large scale background, local fluctuation, etc. The detection for core and filamentary structure and statistics for their physical parameters help us understand the initial condition for star formation.

Herschel's far-infrared observations of thermal radiation from dust provide an unprecedented opportunity to study the substructure of molecular clouds and thereby demystify star formation (e.g., Könyves et al. 2015; Arzoumanian et al. 2019; Zhang et al. 2020). Space telescopes avoid the absorption, distortion and contamination of light by Earth's atmosphere. The detected cores with Herschel can be an order of magnitude more in number than ground-based telescopes (e.g., Könyves et al. 2015; Zhang et al. 2015). Observations with Herschel show that filamentary structures at temperatures around 10–20 K are indeed ubiquitous in the cold ISM. Results from nearby (<500 pc) star-forming molecular clouds survey show that more than 75% of prestellar cores are found in supercritical filamentary structures (linear density $M_{\rm line} > 16 M_\odot\ {\rm pc}^{-1}$) (Könyves et al. 2015) and the typical inner width of the filamentary structure is 0.1 pc which is independent of the column density (Arzoumanian et al. 2011, 2019). In supercritical filaments observations have revealed quasi-periodic chains of dense cores with spacing of 0.15 pc comparable to the filament inner width by Zhang et al. (2020). This implies dense filaments will fragment into gravitationally bound cores, most of which can evolve into stars. The detailed fragmentation manner of the filaments may be controlled by $M_{\rm line}$, geometrical bending, continuous accretion of gas, and magnetic fields (e.g., Zhang et al. 2020).

The distance of Perseus MC is ∼294 pc (Zucker et al. 2019). The overall structure can be divided into north and south parts (see Figure 1). The Perseus MC contains several star-forming dust condensations such as B1, B5, IC 348, NGC 1333, L1455 and L1448 (Zari et al. 2016). About 300 young stellar objects (YSOs) have been identified in Perseus MC (Mercimek et al. 2017). Different from convolving all maps to Herschel's lowest low resolution of 36.″3 and then fitting spectral energy

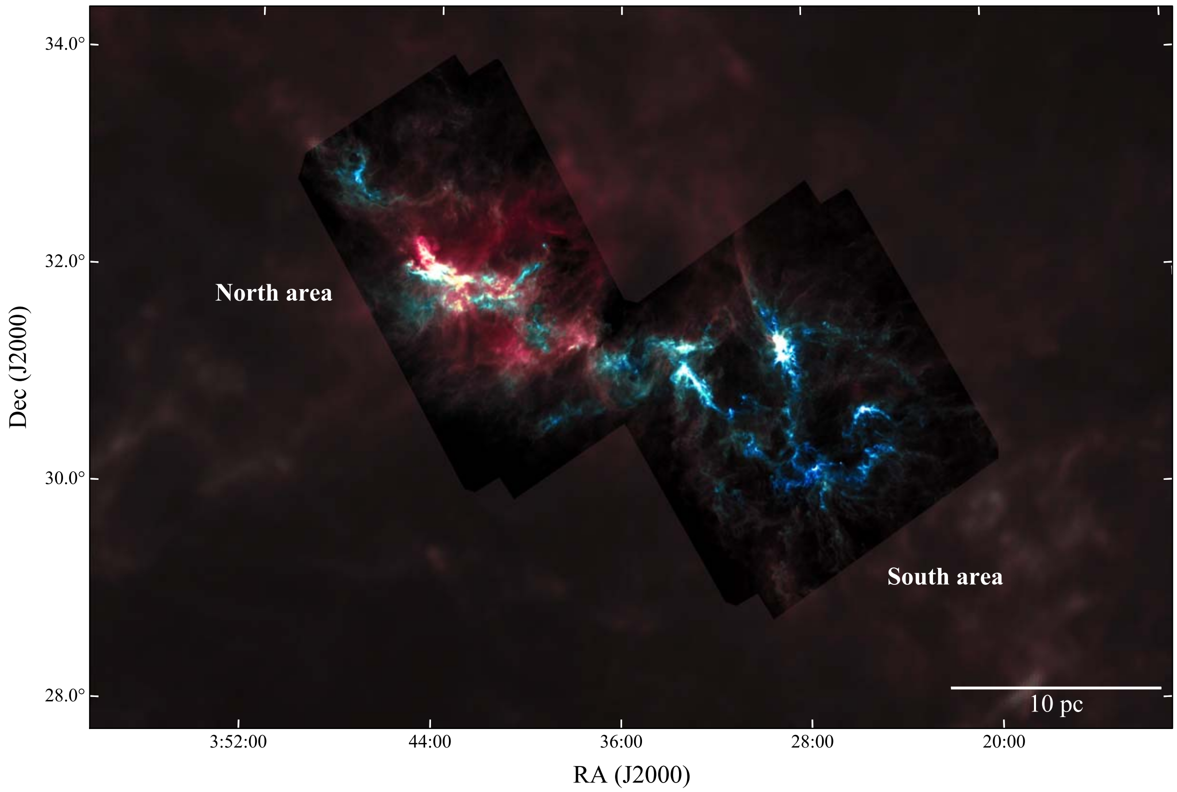

Figure 1. Red–Green–Blue (RGB) composites image showing the 250 μm (blue), 350 μm (green), and 500 μm (red) SPIRE fluxes for the Perseus molecular cloud derived from Herschel and Planck observations. In areas outside the Herschel coverage, dust models were applied to predict the corresponding SPIRE fluxes using Planck/IRAS data. Planck data have a lower resolution than Herschel's, allowing us to identify their spatial boundaries.

distribution (SED) to get a column density map to study Perseus MC, or single-dish low-resolution molecular line mapping (e.g., Ridge et al. 2006; Sadavoy et al. 2014), that resolution is not high enough to get the full sample of cores and filaments, we adopted high-resolution column density images that derived using an improved difference term algorithm that uses all unresolved or slightly resolved structures for enhanced contrast (Men'shchikov 2021b). Latest advances in the methods of multi-scale source and filament extraction: *getsf* (Men'shchikov 2021b), enable us to detect the sources and filamentary network structures in highly complex MC environments and perform statistical analysis on physical parameters such as source luminosity, mass, size, filament width, linear density, curvature etc., as well as exploring the correlation of various parameters.

The outline of the present paper is as follows. In Section 2, we describe the Herschel far-infrared and submillimeter dust emission data of the Perseus MC and give a brief overview of *getsf*. Results are presented in Section 3. In Section 4, we discuss different evolution stages of the north and south of the Perseus MC, core evolution, as well as characteristic physical parameters of filamentary structure. We summarize our conclusions in Section 5.

2. Data Reduction and Observations

2.1. Herschel Archive Data

The Herschel imaging observations of the Perseus molecular cloud include PACS 70 and 160 μm (Poglitsch et al. 2010) and SPIRE 250, 350, and 500 μm (Griffin et al. 2010). The beam sizes of the PACS data at 70 and 160 μm are $8\farcs4$ and $13\farcs5$, respectively. The beam sizes of the SPIRE data at 250, 350, and 500 μm are $18\farcs2$, $24\farcs9$, and $36\farcs3$, respectively. The SPIRE PACS Parallel Mode with a scanning speed of $60'' \, s^{-1}$ is adopted to simultaneously observe this large area of sky in orthogonal mapping directions for the above five bands. We downloaded Herschel maps from ESA Herschel Science Archive.[4] The observed identifiers are 1342190326, 1342190327, 1342214504, and 1342214505. Different from Herschel's high-resolution observations, Planck and IRAS sacrifice resolution for all-sky observations. Planck and IRAS data are set as a reference benchmark, then use the blackbody radiation model to derive the various bands of Herschel, and compare with the Herschel data to obtain the Zero-level offsets. They are 40, 242.9, 96.8, 36.7 and 10.6 MJy sr^{-1} at Herschel 160, 250, 350, and 500 μm,

[4] http://archives.esac.esa.int/hsa/whsa/

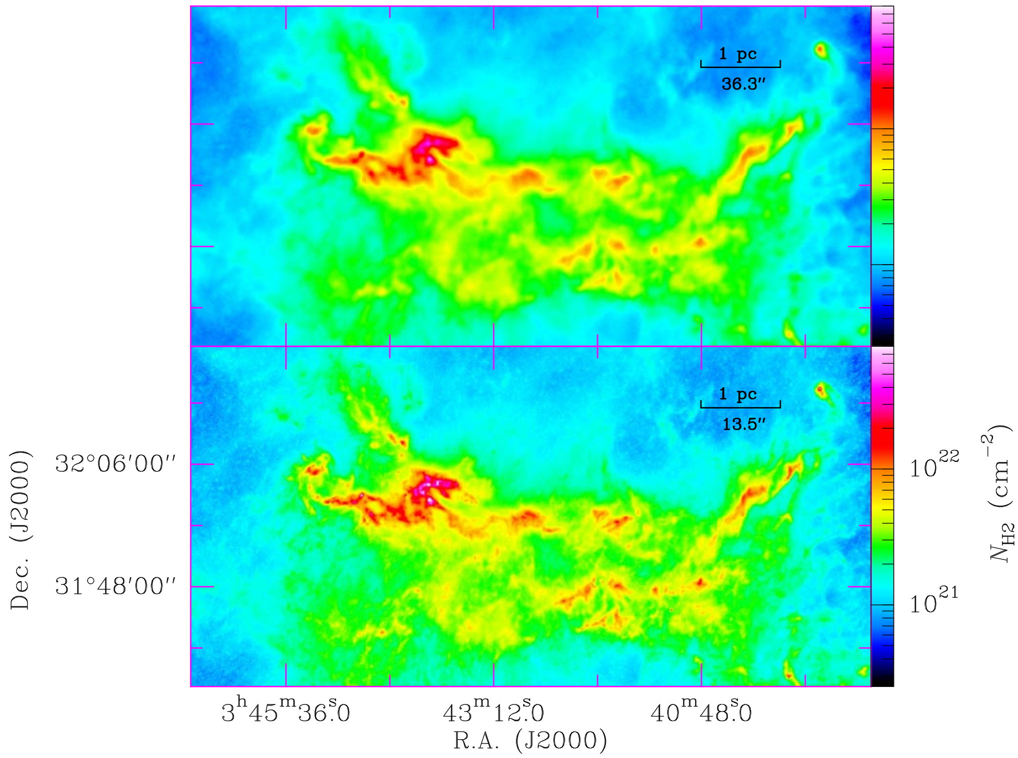

Figure 2. 13.″5 and 36.″3 resolution comparison. The top panel is a column density map with a resolution of 36.″3. The bottom panel is a high-resolution column density image (13.″5) which is derived using an improved difference term algorithm. This algorithm uses all unresolved or slightly resolved structures for enhanced contrast.

respectively in the south region, and −3.2, 37.5, −0.6, −0.9 and −0.1 in the north region. Pixel-by-pixel SED fitting to the Herschel 160–500 μm data with a modified blackbody function was used to create a high-resolution (13.″5) H_2 column density map with the method described in the *getsf* paper (Men'shchikov 2021b). Our column density map has a resolution that is triple as high as the 36.″3-resolution map commonly used in previous studies, and can help us see more details of the MC structure. A comparison is shown in Figure 2.

2.2. Sources and Filamentary Structure Detection Algorithm: getsf

We use *getsf* to extract sources and filaments by separating their structural components in multi-wavelength astronomical images (Men'shchikov 2021b). The algorithm has been validated using a set of benchmark images (Men'shchikov 2021a). Here is a brief introduction of the data processing steps of *getsf*. (1) We need to cut the multi-band dust continuum images observed by Herschel into images with the same pixel size, number of pixels and coordinate system, with *getsf*'s built-in script: *prepobs*. (2) We fit the SED pixel by pixel with *getsf*'s built-in script: *hires*, to obtain a set of column density maps and temperature maps with resolution at Herschel each observed band. (3) *getsf* uses spatial separation techniques to separate the source and filamentary structures from each other and remove their large-scale background. There are also local fluctuations and residual noise in the source and filamentary structure images, and *getsf* will use the flattening technique to remove them. After the above process of background removal and flattening, source and filamentary structures have been cleaned on the single scale images. (4) *getsf* will combine single scales together at each wavelength observed by Herschel. (5) *getsf* will detect location of the sources and the skeleton of the filamentary structures in the combined images. (6) *getsf* will measure properties and create catalog of detected sources and filamentary structures with its built-in script: *smeasure* and *fmeasure*. *getsf* is a almost fully automatic algorithm, and the parameters in the configuration file are the optimal choices after extensive testing. The only user input required is the maximum size of the structure that the user wants to extract.

3. Results

3.1. Physical Environment of Perseus

A high-resolution column density map (13.″5) can be derived, using hires in *getsf*. This map is helpful for better detection and deblending of dense structures. The zero offset level of the north and south regions is very different. Therefore the column density distribution maps of the north and south

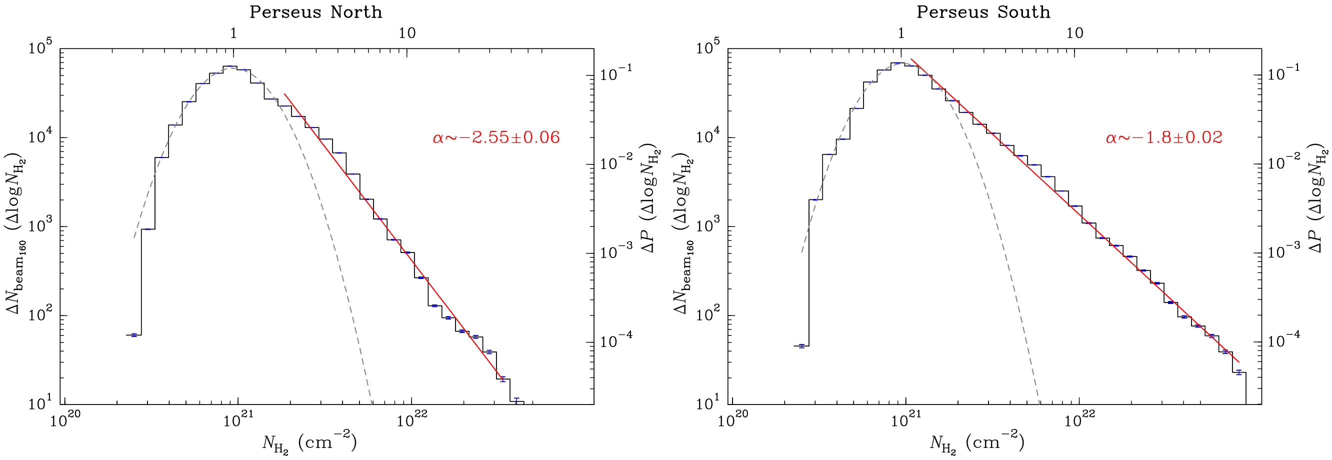

Figure 3. Probability distribution function (PDF) at 13."5 resolution of the column density map in Perseus north and south regions. The lower axis of the horizontal axis is the column density (N_{H_2}), the upper axis of the horizontal axis is the corresponding extinction A_V (mag).

regions are made respectively. The total mass is $\sim 1.2 \times 10^4$ $M_\odot$ obtained by adding up the value of each pixel in the column density map and then multiplying by the mass and weight of the hydrogen molecule. The masses in north and south regions are $\sim 5 \times 10^3$ $M_\odot$ and $\sim 7 \times 10^3$ $M_\odot$ respectively.

The probability distribution function (PDF) can be computed as the histograms of the column density and can be used to characterize physical properties the structure of molecular clouds. The PDF of a variable is a one-point statistics that the relative fraction of the mass in a given range (Vázquez-Semadeni & García 2001). The PDF at 13."5 resolution of the column density map in Perseus north and south regions is shown in Figure 3. The Herschel column density converted to visual extinction units with assumption of $N_{\mathrm{H}_2}(\mathrm{cm}^{-2}) = 0.94 \times 10^{21} A_v$ (mag) (Bohlin et al. 1978). The PDF can be well fitted with parabola and the peak value at $\sim$1 mag. But high density region >2 mag, Perseus north can be well fitted with a power-law with an index of 2.55, and the south region can be well fitted with an index of 1.8. It seems that the power law in the north is steeper than the power law in the south, that means that in the same interval, the south side contains more gas than the north side.

3.1.1. Core Selection

Sufficiently good cores from multi-wavelength catalogs are selected with criteria below, which are based on benchmark tests (Men'shchikov 2021a). We marked all the cores as circles on the column density map (see Figure 4), and four colors of the circles indicate four types of cores. The size of the circles are the geometric mean of core's full width at half maximum (FWHM).

1. $|\mathrm{GOODM}| > 1$, where GOODM is monochromatic goodness.
2. $|\mathrm{SIGNM}| > 1$, where SIGNM is detection significance from monochromatic single scales.
3. $\mathrm{FXP}_{\mathrm{BST}}/\mathrm{FXP}_{\mathrm{ERR}} > 2$, where $\mathrm{FXP}_{\mathrm{BST}}$ is peak intensity and $\mathrm{FXP}_{\mathrm{ERR}}$ is peak intensity error.
4. $\mathrm{FXT}_{\mathrm{BST}}/\mathrm{FXT}_{\mathrm{ERR}} > 2$, where $\mathrm{FXT}_{\mathrm{BST}}$ is total flux and $\mathrm{FXT}_{\mathrm{ERR}}$ is total flux error.
5. $\mathrm{AFWHM}/\mathrm{BFWHM} < 2$, where AFWHM is major size at half-maximum and BFWHM is minor size at half-maximum.
6. $\mathrm{FOOA}/\mathrm{AFWHM} > 1.15$, where FOOA is full major axis of an elliptical footprint.

The cores are classified according to the method described by Könyves et al. (2015). We briefly outline this method here. The integrated flux measured at each wavelength by *getsf* were used to fit an SED with a modified blackbody function, to obtain physical parameters such as mass, temperature, and bolometric luminosity of each core. Prestellar cores are gravitationally bound starless cores most likely to form stars (Ward-Thompson et al. 2007; André et al. 2014). The self-gravitational isothermal equilibrium Bonnor–Ebert (BE) sphere is bounded by surrounding gas, similar to the physical state of the prestellar core. The critical BE mass can be expressed as Bonnor (1956) $M_{\mathrm{BE}}^{\mathrm{crit}} \approx 2.4\, R_{\mathrm{BE}}\, c_s^2/G$, where R_{BE} is the BE radius, and G is the gravitational constant. Assuming an ambient cloud temperature of 10 K, the isothermal sound speed c_s is $\sim$0.2 km s^{-1}. We use this model to select prestellar cores. The core size is defined as the mean deconvolved FWHM diameter at the resolution of 18."2 of an equivalent elliptical Gaussian source: $R_{\mathrm{dec}} = \sqrt{\mathrm{AFWHM} \,*\, \mathrm{BFWHM} - \theta_{18''2}^2}$, where $\theta_{18''2}$ is the

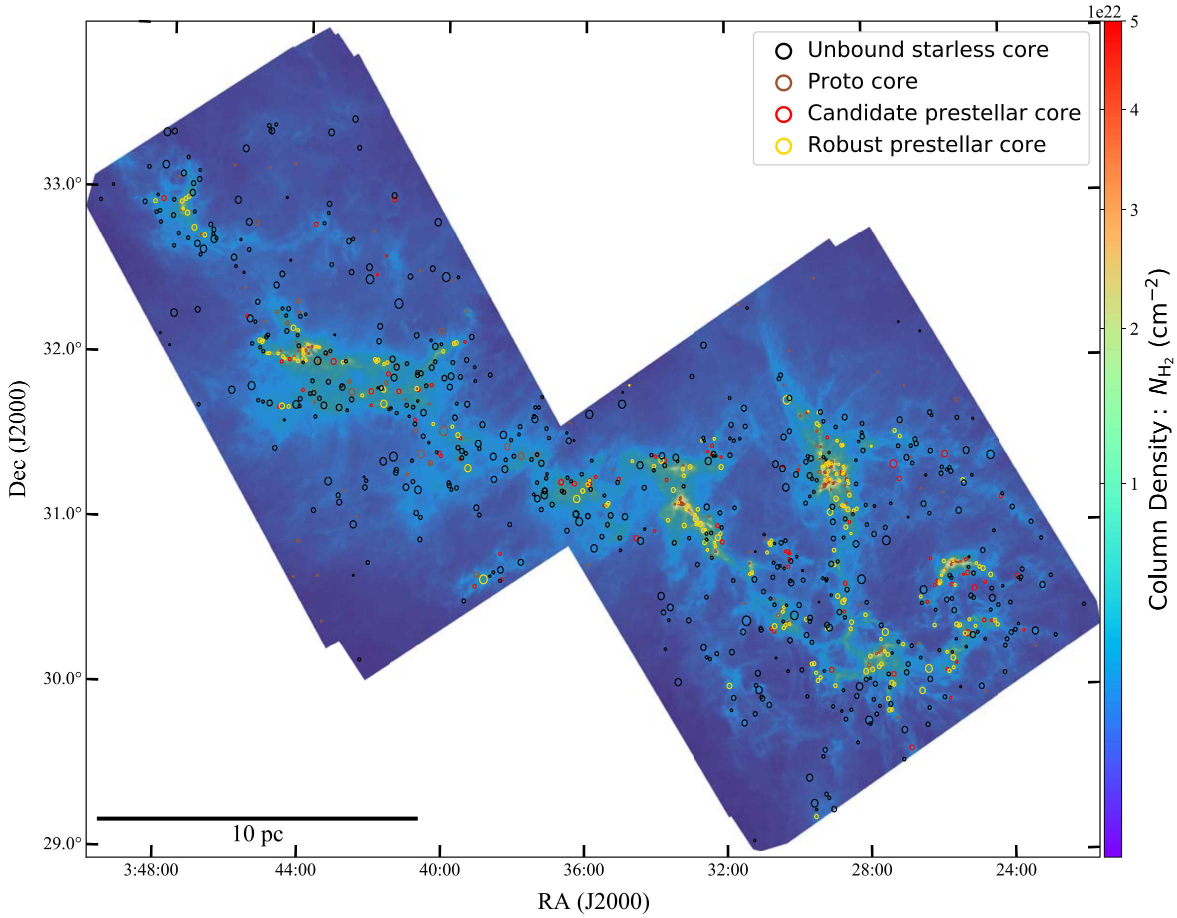

Figure 4. Positions of the 952 dense cores identified in the Perseus overlaid on the Herschel high resolution 13″.5 column density map. Black, brown, red, and yellow circles mark the 536 unbound starless cores, the 130 protostellar cores, the 87 candidate prestellar cores, the 199 robust prestellar cores, respectively. The size of the circle is the geometric mean of the core's FWHM.

angular resolution at Herschel 250 μm band. If the ratio $\alpha_{\rm BE} = M_{\rm BE}^{\rm crit}/M_{\rm core} \leqslant 2$, we deem that this starless core is self-gravitating and classified as a robust prestellar core. Könyves et al. (2015) propose an empirical size-dependent ratio $\alpha_{\rm BE,emp} \leqslant 5 \times (\sqrt{\rm AFWHM \ * \ BFWHM}/\theta_{18''2})^{0.4}$ is also considered to select candidate prestellar cores. Cores with at least one protostar in the half-power column density profile are considered to be protostellar cores.

3.1.2. Statistics of Core Physical Parameters

We obtained physical parameters, which include temperature, bolometric luminosity and mass by using SED fitting for each core. Statistical and fitting results of all the cores show in Figures 5 and 6. Figure 5 shows histograms of core temperature, mass, bolometric luminosity and radius. We obtained 12.48 K for median value of temperature, 0.16 $M_\odot$ for mass, 0.06 $L_\odot$ for bolometric luminosity and 40″.28 for radius.

Figure 6 shows the correlation of each parameter, and blue, black, green and purple markers represent for robust prestellar cores, candidate prestellar cores, unbound starless cores and proto cores, respectively. Figures 6(a) and (d) show the definitely linear correlation ($R_a^2 = 74.9\%$, $R_b^2 = 79.4\%$) of temperature and mass or ratio of mass to temperature and ratio of mass to luminosity. However, Figures 6(b) and (c) show both temperature and mass are independent of bolometric luminosity.

3.2. Filamentary Structure Sample

3.2.1. Filamentary Structure Selection

We use the built-in script *getsf*: *fmeasure* to measure the filamentary structure along its skeleton on the background-subtracted 13″.5 resolution column density image of the filament components. Filamentary structures are three-dimensional structures in space, but what Herschel observed are their two-dimensional projections. Filamentary structures are twist in

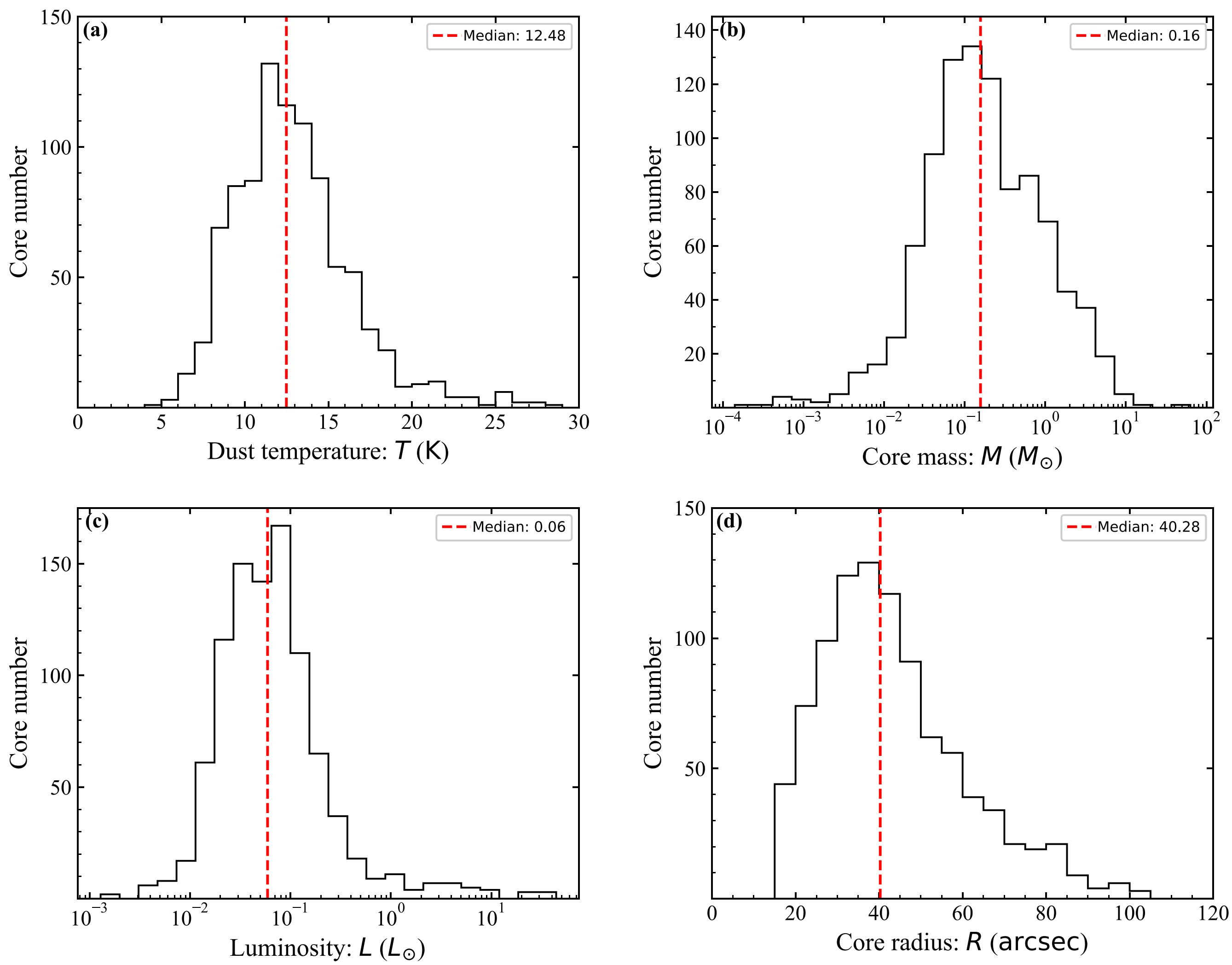

Figure 5. Histogram of physical parameters of the cores. Panels (a), (b), (c) show core dust temperature, mass and bolometric luminosity obtained from SED fitting. Panel (d) is the geometric mean of the core FWHMs. The red dashed lines mark the median value.

shape. They blend with themselves and with the surrounding structures. The column density contrast (C) of the filamentary structure is defined as $C = N_{\rm H_2}^{\rm crest}/N_{\rm H_2}^{\rm bg}$, where $N_{\rm H_2}^{\rm crest}$ is the filament crest column density and $N_{\rm H_2}^{\rm bg}$ is the filament crest background. To choose a clear structure we first select structures with $C > 0.5$ from the skeleton network. This resulted in a sample with 500 segments in the Perseus north region and 596 segments in the Perseus south region.

The beginning and end of filamentary structures are not easily objectively determined. They have substructures, and it is not easy to determine which are substructures and which are the main structures. So as to simplify this complex problem, the strategy adopted in *getsf* by splitting the skeleton network into single segments. Although, to some extent, the length of the filamentary structures is not objective. However, the longer the segment is, the more likely it is to be a filamentary structure, which is beyond doubt. In order to further improve the reliability of the sample, we select structures with segment length: $L > 0.2$ pc from the above sample of $C > 0.5$. This resulted in a sample with 162 segments in the Perseus north region and 229 segments in the Perseus south region.

3.2.2. Statistics of Physical Parameters of Selected Filamentary Structures

fmeasure uses two methods to obtain the linear density ($M_{\rm line}$) of the filamentary structures. One of the method is that *fmeasure* derives the mass ($M_{\rm fil}$) of a filamentary structure by directly integrating its footprint and then get $M_{\rm line}$ by $M_{\rm line} = M_{\rm fil}/L_{\rm fil}$, where $L_{\rm fil}$ is filament length and filament footprint is defined as the area between the skeleton and the

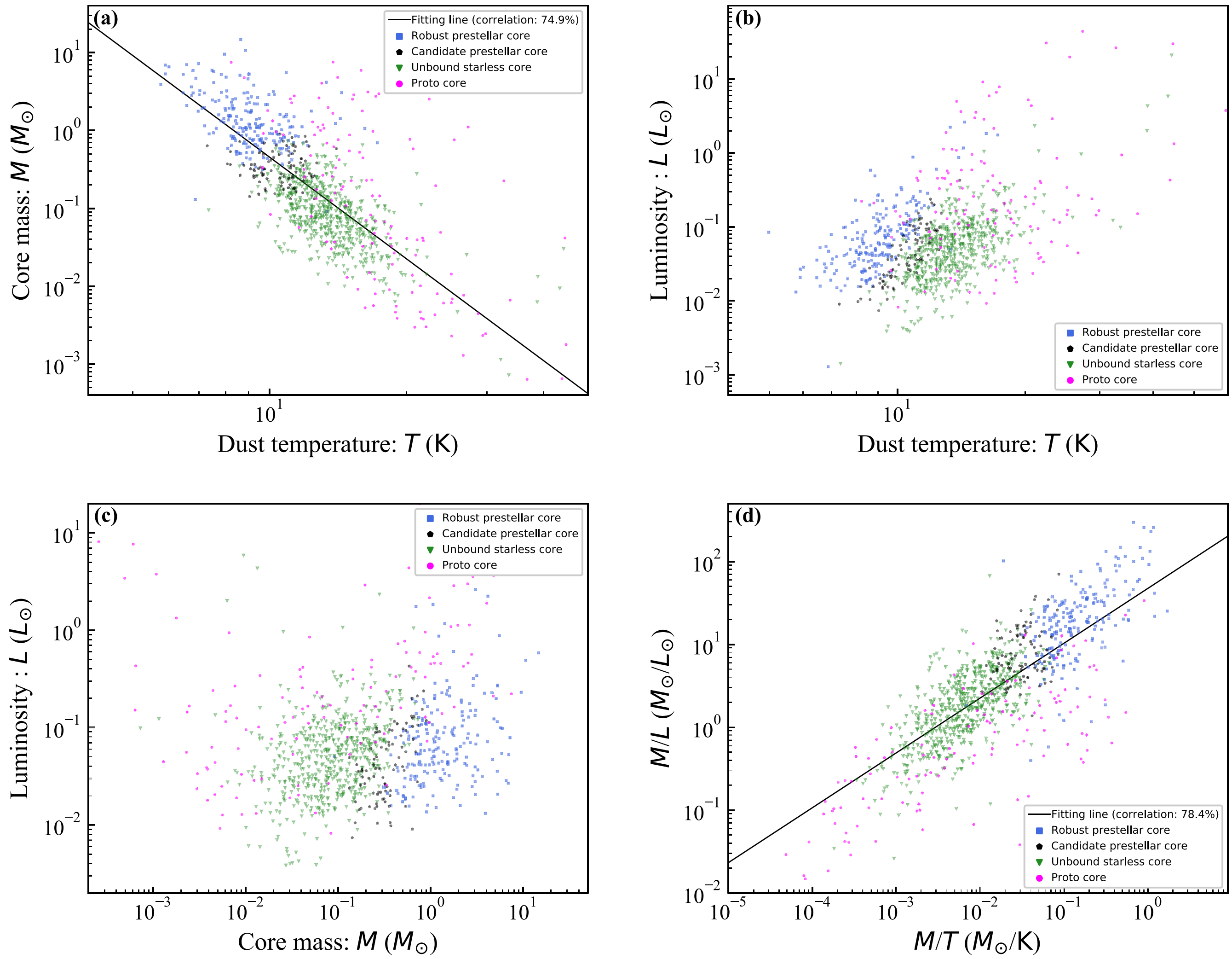

Figure 6. Correlations among core physical parameters derived by SED fitting. (a) A clear correlation between core dust temperature and mass, $\log_{10}(M/M_\odot) = -4.34\log_{10}(T/\mathrm{K}) + 4$. (b), (c) Core luminosity has no significant correlation with dust temperature and mass. (d) A clear correlation between M/L and M/T, $\log_{10}(M/T) = 0.66\log_{10}(M/T) + 1.67$.

largest extent on each side. Another way is that density integration can be performed at any sampling point along the crest, and this integral is $M_{\rm line}$ of this sampling point. We can use $M_{\rm line}$ median value of all sampling points as $M_{\rm line}$ of this filamentary structure.

We drew all the filamentary network structure selected with contrast $C > 0.5$ in Figure 7, and the color of the filaments represent the intensity of linear density. The filament of whiter the color means higher linear density. In Figure 8, we counted the parameters of the filaments in the north and south regions respectively, and made histograms, in which the blue bars represent all the filaments and orange bars represent high reliable filaments. Figures 8(a), (c), (e) show the length, width and linear density of filaments in the north region, then (b), (d), (f) show the parameters in the south region. From the median value, the length of filaments in the south region is greater than that of the north region and the width of the filaments contrast between the north and south regions is just the opposite. Although the linear density of filaments in the south is slightly lower than that in the north, it is obvious that the supercritical ($M_{\rm line} > 16\,M_\odot\,\mathrm{pc}^{-1}$) filaments are more distributed in the south region. Figure 9 shows the correlation of the filaments between column and linear density or column density and width. Figures 9(a), (b) suggest clear correlation ($R_a^2 = 92.5\%$, $R_b^2 = 95.9\%$) of column density and linear density whether in the South or the north region. However (c), (d) show that column density are uncorrelated with width, and most (80%) width of filaments are distributed in gray areas. The blue dotted lines represent the median value, with 0.17 and 0.12 pc on the north and south regions. Table 1 reports the core fractions found in and not in filaments. Filament segments are simply divided into three categories: $M_{\rm line} > 16$, $8 < M_{\rm line} < 16$

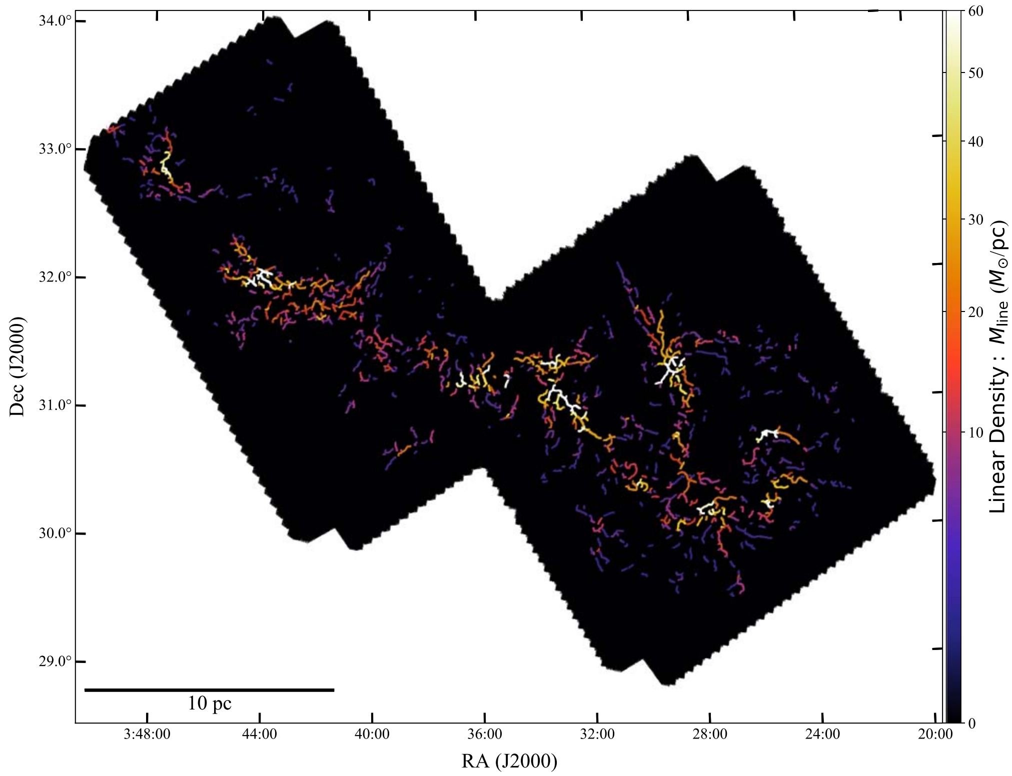

Figure 7. Perseus filamentary network structures selected with contrast $C > 0.5$. The linear density ($M_{\rm line}$) of the filamentary structure is only taken on the narrow side to avoid contamination as much as possible.

Table 1
Fractions of Cores Found Inside the Filamentary Structures

Linear Density	Unbound Starless	Candidate Prestellar	Robust Prestellar	Protostellar
$M_{\rm line} > 16$	57 (10.6%)	26 (29.9%)	135 (67.8%)	66 (50.8%)
$8 < M_{\rm line} < 16$	62 (11.6%)	19 (21.9%)	36 (18.1%)	10 (7.7%)
$M_{\rm line} < 8$	172 (32.1%)	28 (32.2%)	19 (9.5%)	6 (4.6%)
Not in filament	245 (45.7%)	14 (16.1%)	9 (4.5%)	48 (37.0%)

and $M_{\rm line} < 8$. A core is considered to be inside a filament segment if 50% of its footprint is on the associated filament segment. The fractions of unbound starless cores decreases with $M_{\rm line}$, but the fractions of robost prestellar and protostellar cores increase with $M_{\rm line}$. Many unbound starless cores (∼45%) are free outside the filament. The supercritical filamentary structure mainly wraps the prestellar and protostellar cores.

4. Discussion

4.1. The Evolution Stages of the North and South are Different

The thickness of the molecular cloud traced by different probes is different in the direction of sight. This results in different density distributions detected by different probes of molecular cloud. But in general, there is a rapidly decreasing trend of PDF at the high density range. This can deduced that the dense structures occupy only a small fraction of the volume of the molecular clouds and most of the volume is filled with low density background gas.

For isothermal, supersonic, turbulent gases, shock produces a random density enhancement proportional to the mean density. According to the central limit theorem, the PDF is a lognormal function (Vazquez-Semadeni 1994). PDF should be made only for those contours that are closed in the map. In numerical simulation, cloud boundaries are generally equivalent to non-closed density contours in numerical boxes. The range of these column densities is underestimated, resulting in spurious drops in the PDF. The PDF of the molecular cloud does not necessarily decrease at low densities, and inferring

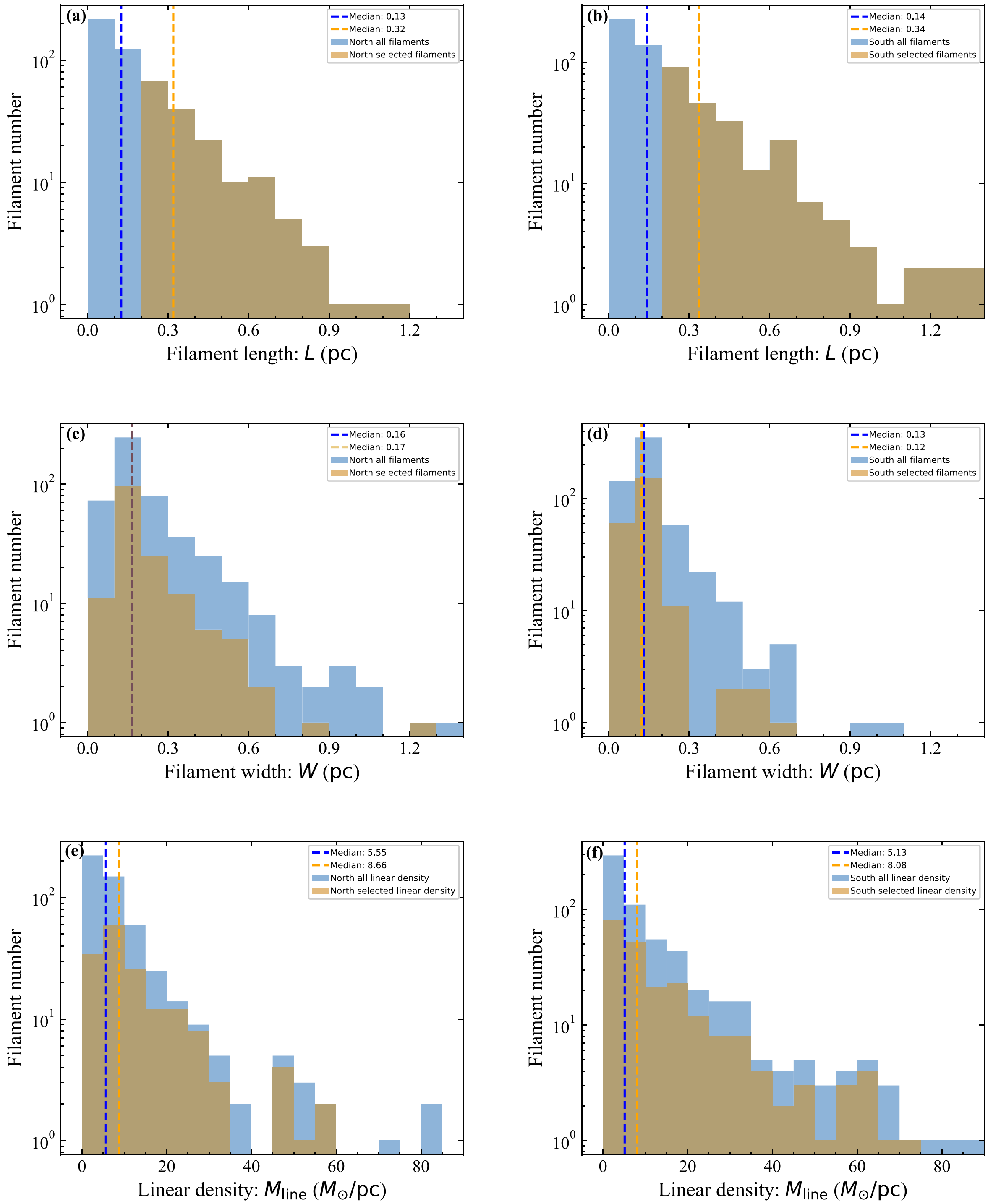

Figure 8. Histogram of physical parameters of the filamentary structures. In this set of histograms, the sample "all" are the filamentary structures with $C > 0.5$; the sample "selected" are the filamentary structures with $C > 0.5$ and $L > 0.2$ pc. We conduct separate statistics for filamentary structure in the north and south regions.

the physical properties of the molecular cloud by fitting the low-density region of the PDF may be wrong. Therefore, great care should be taken when extrapolating the PDF shape of the cloud in the numerical simulation to the real observation data (Alves et al. 2017). The background component of the molecular cloud that exhibits a log-normal function is uncorrelated with specific star formation activity. However, the PDF dense component exhibits a power-law distribution

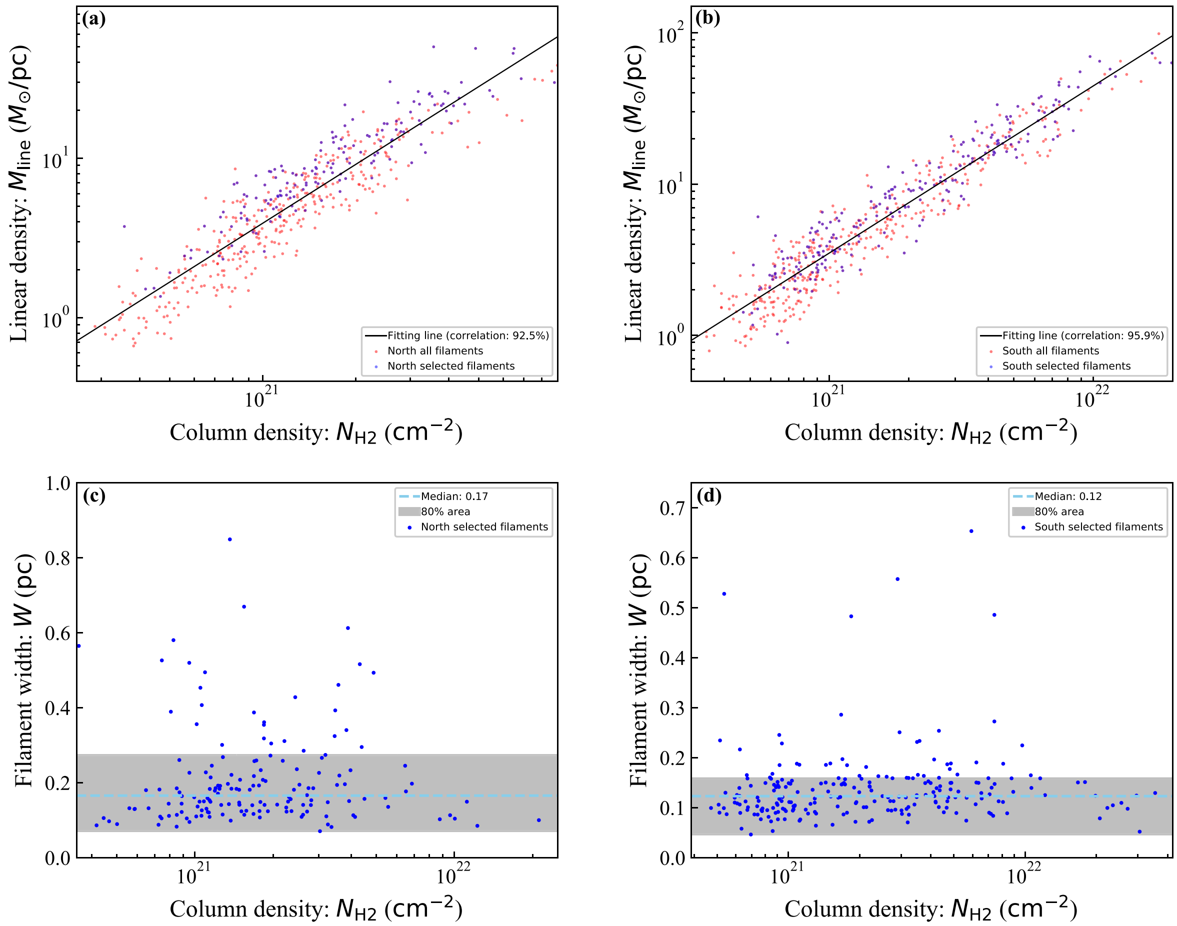

Figure 9. Crest column density (N_{H_2}) of filamentary structures as a function of linear density (M_{line}) and width (W) in the north and south regions of Perseus molecular cloud. N_{H_2} and M_{line} are clearly related. N_{H_2} are uncorrelated with W by three orders of magnitude from $\sim 10^{20}$ to $\sim 10^{22}$ cm^{-2}.

that is closely related to star formation (Kainulainen et al. 2009). Numerical simulations predict that turbulence dominates the lognormal distribution, while gravity leads to a power-law form (Kritsuk et al. 2011). The Perseus south region shows a power law with an exponent of −1.8. The Perseus north region has an exponent of −2.55. The Perseus south region is flatter than the Perseus north region and closer to power law exponent of −1.35 for stellar initial mass function proposed by Salpeter (1955).

The gravitational potential energy is $\Omega = -\alpha \frac{GM^2}{R}$, where α is fudge factor of order unity that depends on the internal density structure. M is the observed structure mass, and R is the effective radius. The 3σ noise level is $\sim 2 \times 10^{21}$ cm^{-2}, which was estimated at regions without sources. The masses of gas component with $N_{H_2} > 3\sigma$ are $\sim 1.8 \times 10^3 M_\odot$ and $\sim 3.3 \times 10^3 M_\odot$ at north and south regions respectively, and the effective radii are 2.8 and 3.2 pc. The Ω at the north region is $1.2 \times 10^6 \alpha G\ M_\odot^2$ pc^{-1}, and the Ω at the south region is $3.4 \times 10^6 \alpha G\ M_\odot^2$ pc^{-1}. Assuming that the south and north regions have the same α value, the gravitational force of Perseus in the south region is about three times stronger than that in the north.

Perseus MC is a medium active star-forming region. (Mercimek et al. 2017) identified 222 YSOs in Perseus MC. Number of YSOs per unit area that is similar to NGC 2264, but higher than Orion B and lower than Ophiuchus (Pokhrel et al. 2020). The number of YSOs (153) in south region is significantly more than that in the north region (69). Most of the YSOs in the south region are class II/III, and the evolution stage is obviously later than that in the north region.

Because the gas and dust will block the photon radiation, the denser region of gas and dust in the molecular cloud will show lower temperature. We checked the temperature map officially released by Planck and found that there is a clear temperature difference between the north and south regions. The dust temperature of large-scale background gas of the north region is at 18 K. Dense gas components ($N_{H_2} > 3\sigma$) are closely related to star formation. IC 348 reflection nebula reaches 20–24 K, which covers 70% of the area of dense gas component in the north region. The dust temperature of large-scale background gas of the south region is at 17 K. Dust temperature of dense gas component is about 14–15 K in the south region. Dust temperature as an indicator to characterize the difference between the two regions, which have a temperature difference of about 5 K in two regions for these dense gas components. To conclude, differences in PDF power law exponent of the PDF, gravity, number of YSOs, and dust temperature indicate that the evolution stages of the north and south regions of Perseus MC are different.

4.2. Core Evolution

Core dust temperatures are strongly correlated with masses and M/L is strongly correlated with M/T. Our results are similar to those of previous studies, such as Marsh et al. (2014, 2016), which show that central temperature was linearly negatively correlated with masses of starless and prestellar cores in Taurus, and confirmed a more stronger correlation with peak column density. An intuitive explanation is that as the strength of the shielding core from interstellar radiation field increases, the temperature will decrease and the mass will increase, in theory, which may be explained by blackbody radiation. Assuming dust radiation is optically thin at a certain frequency the measured fluxes can be written as:

$$f_\nu = B_\nu(T)\,\kappa_0(\nu/\nu_0)^{\beta}\eta M D^{-2}. \tag{1}$$

For a core at a distance D and measured flux f_ν at a certain frequency ν, the luminosity at this ν is

$$L_\nu = 4\pi D^2 f_\nu. \tag{2}$$

Bolometric luminosity $L_{\rm bol}$ is the luminosity of a core measured over all frequency, which is derived by:

$$L_{\rm bol} = 4\pi D^2 \int f_\nu\, d\nu. \tag{3}$$

Then

$$M/L_{\rm bol} \sim \frac{M}{D^2 \,*\, \int f_\nu\, d\nu}. \tag{4}$$

And

$$\int f_\nu\, d\nu \sim \nu_{\rm peak} \,*\, {\rm SED}_{\rm peak}. \tag{5}$$

Then according to Wien's law: $\nu_{\rm peak} \sim T$, we can deduce that $M/L_{\rm bol} \sim M/T$.

4.3. Physical Properties of Ubiquitous Filamentary Structures

Herschel observations show that filamentary structures are indeed ubiquitous in the molecular cloud (e.g., Men'shchikov et al. 2010; Hill et al. 2011). In the nearby clouds (<500 pc), filaments profiles measured on the Herschel column density map in the radial direction show a typical inner width ∼0.1 pc and no wider than ∼0.2 pc (Arzoumanian et al. 2011, 2019). The origin of the typical inner width of filamentary structures remains a controversial topic. There are currently three explanations for typical inner width. The gravitational and thermal pressure equilibrium of the isothermal gas results in this typical inner width of 0.1 pc with a weak dependence on column density. Typical inner width is just a result of the mechanical equilibrium in thermodynamics in radial direction (Fischera & Martin 2012). An alternative explanation is that the filaments originate from plane-intersecting shock waves due to supersonic interstellar turbulence, and that the filament width corresponds to the (magneto-)sonic scale (Pudritz & Kevlahan 2013). Finally, another possible explanation is that the typical inner width of the filament may be set by a dissipation mechanism, magnetohydrodynamic (MHD) waves induced by ion-neutral friction (Hennebelle 2013). The width measured with selected filamentary structure with $L > 0.2$ pc and $C > 0.5$, has higher confidence than the entire filamentary network. This sample includes 162 segments in the Perseus north region and 229 segments in the south region. The width median value in the north region is 0.17 and 0.12 pc in the south region. Large-scale diffuse gas is more abundant in the north than in the south. The blending in the north is more severe, and the measured width is wider than the south. The measurement of width is consistent with the typical inner width of the filamentary structure is 0.1 pc measured by Arzoumanian et al. (2011, 2019).

Supercritical filamentary structures play an important role in star formation. Stars are formed in molecular filaments with linear masses equal to or greater than the critical linear mass (e.g., André et al. 2014). The critical linear mass of an isothermal cylindrical filamentary structure depends on temperature and mean molecular weight. Mean molecular weight in turn depends on the metallicity, which in turn can have a dependence on the location in the Galaxy. If we adopt 10 K of ambient cloud temperature and 2.8 of mean molecular weight, the critical line mass should be 16 $M_\odot$ pc^{-1}. We find ∼70% of robust prestellar cores (135/199) embedded in supercritical filaments which implies that the gravitationally bound cores come from fragmentation of supercritical filaments.

5. Conclusions

With the latest improved difference term algorithm: hires, we made a high-resolution (13″.5) column density map for Perseus MC with Herschel multi-wavelength dust continuum maps, and detected the source and filamentary structure using a new spatial decomposition method: *getsf*, and performed statistics on measured physical parameters so as to better understand the initial conditions of the star formation in the molecular cloud. Our findings can be summarized as follows:

1. We find power-law distribution in PDF of the Perseus south region is flatter than the north region, and the

average temperature of dense gas component with $N_{H_2} > 3\sigma$ in the south region is about 5 K lower than the north region, and the number of YSOs in the south is significantly less than that in the north. Those observational evidences imply that the south region is more gravitationally bound than the north region and suggests that evolution stages are different in two regions.

2. We selected 952 reliable cores from original source catalog detected by *getsf*, and divided them into four groups: 536 unbound starless cores, 87 candidate prestellar cores and 199 robust prestellar cores, 130 protostellar cores. We find that M is strongly correlated with T and M/L is strongly correlated with M/T, which is in line with the prediction of the blackbody radiation. These two correlations show a clear evolutionary sequence from unbound starless cores to robust prestellar cores.
3. We find that crest N_{H_2} of the filamentary structures is clearly related with $M_{\rm line}$, and is uncorrelated with W by three orders of magnitude from $\sim 10^{20}$ to $\sim 10^{22}$ cm^{-2}. We find ~70% of robust prestellar cores (135/199) embedded in supercritical filaments with $M_{\rm line} > 16\,M_\odot\,{\rm pc}^{-1}$, which implies that the gravitationally bound cores come from fragmentation of supercritical filaments.

Acknowledgments

This work is supported by the Ministry of Science and Technology of China through grant 2010DFA02710, the Key Project of International Cooperation, and by the National Natural Science Foundation of China through Grant Nos. 11503035, 11573036, 11373009, 11433008, 11403040 and 11403041. Guoyin ZHANG acknowledges support from China Postdoctoral Science Foundation (No. 2021T140672), and the National Natural Science Foundation of China (No. U2031118).

References

Alves, J., Lombardi, M., & Lada, C. J. 2017, A&A, 606, L2
André, P., Di Francesco, J., Ward-Thompson, D., et al. 2014, in Protostars and Planets VI, ed. H. Beuther et al. (Tucson, AZ: Univ. of Arizona Press), 27
Arzoumanian, D., André, P., Didelon, P., et al. 2011, A&A, 529, L6
Arzoumanian, D., André, P., Könyves, V., et al. 2019, A&A, 621, A42
Bergin, E. A., & Tafalla, M. 2007, ARA&A, 45, 339
Bohlin, R. C., Savage, B. D., & Drake, J. F. 1978, ApJ, 224, 132
Bonnor, W. B. 1956, MNRAS, 116, 351
Fischera, J., & Martin, P. G. 2012, A&A, 547, A86
Griffin, M. J., Abergel, A., Abreu, A., et al. 2010, A&A, 518, L3
Hennebelle, P. 2013, A&A, 556, A153
Hill, T., Motte, F., Didelon, P., et al. 2011, A&A, 533, A94
Kainulainen, J., Beuther, H., Henning, T., & Plume, R. 2009, A&A, 508, L35
Könyves, V., André, P., Men'shchikov, A., et al. 2015, A&A, 584, A91
Kritsuk, A. G., Norman, M. L., & Wagner, R. 2011, ApJL, 727, L20
Marsh, K. A., Griffin, M. J., Palmeirim, P., et al. 2014, MNRAS, 439, 3683
Marsh, K. A., Kirk, J. M., André, P., et al. 2016, MNRAS, 459, 342
Men'shchikov, A. 2021a, A&A, 654, A78
Men'shchikov, A. 2021b, A&A, 649, A89
Men'shchikov, A., André, P., Didelon, P., et al. 2010, A&A, 518, L103
Mercimek, S., Myers, P. C., Lee, K. I., & Sadavoy, S. I. 2017, AJ, 153, 214
Poglitsch, A., Waelkens, C., Geis, N., et al. 2010, A&A, 518, L2
Pokhrel, R., Gutermuth, R. A., Betti, S. K., et al. 2020, ApJ, 896, 60
Pokhrel, R., Myers, P. C., Dunham, M. M., et al. 2018, ApJ, 853, 5
Pudritz, R. E., & Kevlahan, N. K. R. 2013, RSPTA, 371, 20120248
Ridge, N. A., Di Francesco, J., Kirk, H., et al. 2006, AJ, 131, 2921
Sadavoy, S. I., Di Francesco, J., André, P., et al. 2014, ApJL, 787, L18
Salpeter, E. E. 1955, ApJ, 121, 161
Vazquez-Semadeni, E. 1994, ApJ, 423, 681
Vázquez-Semadeni, E., & García, N. 2001, ApJ, 557, 727
Ward-Thompson, D., André, P., Crutcher, R., et al. 2007, in Protostars and Planets V, ed. B. Reipurth, D. Jewitt, & K. Keil (Tucson, AZ: Univ. of Arizona Press), 33
Zari, E., Lombardi, M., Alves, J., Lada, C. J., & Bouy, H. 2016, A&A, 587, A106
Zhang, G., Li, D., Hyde, A. K., et al. 2015, SCPMA, 58, 5561
Zhang, G.-Y., André, P., Men'shchikov, A., & Wang, K. 2020, A&A, 642, A76
Zhang, G.-Y., Xu, J.-L., Vasyunin, A. I., et al. 2018, A&A, 620, A163
Zucker, C., Speagle, J. S., Schlafly, E. F., et al. 2019, ApJ, 879, 125